

Direct measurements of the properties of Thick-GEM reflective photocathodes

M. Baruzzo^{a,1}, C. Chatterjee^b, P. Ciliberti^b, S. Dalla Torre^a, S.S. Dasgupta^{b,2}, B. Gobbo^a, M. Gregori^a, G. Hamar^{c,*}, S. Levorato^a, G. Menon^a, C. A. Santos^a, F. Tessarotto^a, Triloki^{a,3}, D. Varga^c, Y. X. Zhao^a

^aINFN Sezione di Trieste, Trieste, Italy

^bUniversity of Trieste and INFN Sezione di Trieste, Trieste, Italy

^cWigner Research Centre for Physics, Budapest, Hungary

^dPhysics Department, University of Aveiro, Aveiro, Portugal

Abstract

In the context of the development of novel Thick GEM based detectors of single photons, the high resolution optical system, nicknamed Leopard, providing a detailed surface scanning of the Thick GEM electron multipliers, has been used for a set of systematic measurements of key Thick GEM properties. These results are reported and discussed. They confirm by direct observation Thick GEM properties previously inferred by indirect measurements and answer to relevant questions related to the use of Thick GEMs as photocathode substrates in novel gaseous photon detectors.

Keywords: Thick GEM, UV Photon detector, High resolution scan

Contents		6 Charging-up aspects	6
1 Introduction	2	6.1 The time evolution of the gain in THGEM multipliers	6
2 The THGEM electron multiplier	2	6.2 Gain time evolution observed with the Leopard setup	7
3 The THGEM-based photocathodes of the photon detectors for the upgrade of COMPASS RICH-1	3	7 Gain studies	7
4 Equipment and setup	4	7.1 Gain uniformity by comparing single hole gain	7
4.1 The scanning system and the setup . . .	4	7.2 Gain uniformity versus radial distance from the hole centre	7
4.2 The control and data acquisition system of the scanning system	4	8 Photoelectron extraction studies	8
4.3 The measured thick GEMs	5	8.1 The effective quantum efficiency in gaseous detectors	8
5 Measurement procedures	5	8.2 Direct observation of the effective quantum efficiency using THGEM as photocathode substrate	9
5.1 Algorithms for gain and yield extraction	5	8.3 Comparison of the photoelectron extraction in THGEMs with different geometry.	10
5.2 Image focusing	6	9 Photoelectron extraction from CsI and from gold in gaseous atmosphere	11
5.3 Estimation of the errors	6	10 Conclusions	12

*Corresponding author. E-mail address: gergo.hamar@ts.infn.it (G.Hamar)

¹present address: University of Udine, Udine, Italy and INFN, Sezione di Trieste, Trieste, Italy

²on leave from Matrivani Institute of Experimental Research and Education, Kolkata, India

³also at Abdus Salam ICTP, Trieste, Italy

1. Introduction

The first generation of gaseous photon detectors with solid state photocathode are the MultiWire Proportional Chambers (MWPC) coupled to a CsI photocathode[1]. Novel gaseous photon detectors must represent a progress in the field and thus they must match two basic requirements, namely reduced rates of photon backflow and of Ion BackFlow (IBF) to the photocathode. These reduced rates help to overcome the photocathode ageing, make possible high gain operation and intrinsically fast detector operation. Essentially, an achievement of detectors with high rate capabilities. Recently developed Micro Pattern Gaseous Detectors (MPGD) look promising concerning both of these issues. Gas Electron Multiplier (GEM)[2] and GEM-derived multipliers, as THick GEMs (THGEM)[3], are intrinsic fast devices. In fact, the signal is mainly generated by the electron motion. In MICROMEGAS (MM)[4], in spite of the parallel plate structure, the signal development is fast thanks to the extremely thin cathode-anode gap. Concerning the suppression of the photon and ion backflow, in multilayer GEM and THGEM structures, no photon feedback is present, while a good fraction of the ions is trapped in the intermediate layers and do not reach the photocathode; in particular dedicated studies of the IBF rates have been performed due to the interest not only for photon detection[5], but also for the use of GEMs as TPC read-out elements[6]. In MMs, the ions created in the multiplication process are naturally trapped in the multiplication gap thanks to the large unbalance of the electric field above and below the micromesh which defines the amplification region.

The concept of MPGD-based photon detectors had a first application in the threshold Cherenkov counter Hadron Blind Detector (HBD)[7] of the Phenix experiment: the photon detectors are triple GEM counters where the first GEM foil, coated with a CsI film, is used as reflective photocathode; the detectors are operated at a low gain level (4000), not adequate for efficient single photon detection. Thanks to the observed high gain, THGEMs have been proposed for novel gaseous detectors of single photons[8] and relevant R&D studies have been performed[5, 9, 10, 11, 12]. THGEMs can be used in multilayer arrangements or coupled to a MM multiplication stage, as it is the case for the upgrade of the COMPASS RICH. In all these architectures the photocathode substrate is a THGEM plate. In this context, the opportunity of mapping the THGEM response to single UV photons offers a handle of great relevance for understanding the behavior of THGEM photocathodes. These studies are made possible by the system

for the high resolution surface scanning of THGEMs by single photo-electron detection, nicknamed Leopard, recently introduced[13] (Sec.4.1). A number of central questions related to the development of THGEM based novel photon detectors have been answered thanks to the Leopard capability to provide detailed gain and efficiency maps.

This article is dedicated to a first set of systematic studies of THGEM multipliers, which are introduced in Sec. 2, while the THGEMs used as photocathodes for the upgrade of the COMPASS RICH are described in Sec. 3. The measurements have been performed by the Leopard system, described together with the overall experimental setup in Sec. 4; the measurement procedures are given in Sec. 5, while the results about gain and photoelectron extraction are presented and discussed in Secs. 7 and 8, respectively. These studies are performed converting the light in the gold coating of the THGEM PCB surface. Dedicated measurements reported in Sec. 9 allow to extend the results concerning photoelectron extraction from gold to photoelectron extraction from CsI. Conclusions are presented in Sec. 10.

2. The THGEM electron multiplier

THGEMs, introduced in parallel by several groups[3], are electron multipliers derived from the GEM design, scaling the geometrical parameters and changing the production technology. The Cu-coated polyimide foil of the GEM multipliers is replaced by standard PCBs and the holes are produced by drilling. The conical shape of the GEM holes that forms uncoated polyimide rings around the holes themselves are replaced by a clearance ring, the rim, surrounding the hole and obtained by Cu etching. The hole arrangement is similar to the one adopted for the GEMs; the circular hole centres are distributed according to a repetitive pattern: the basic cell is an equilateral triangle. Typical values of the geometrical parameters are PCB thickness of 0.2-1 mm, hole diameter ranging between 0.2 and 1 mm, hole pitch of 0.5-1.2 mm and rim width between 0 and 0.1 mm (Fig.1). The early phase of the THGEM characterisation was largely contributed by the Weizmann group led by A. Breskin[8]. In this context, large gains along with good rate capabilities have been reported for single or double THGEM layers.

THGEMs can be produced in large series and large size with standard PCB technology, instead of large number of holes present, few millions per square meter. THGEMs have intrinsic mechanical stiffness, and they are robust against damages produced by electrical

discharges. Due to the technology used, the material budget of THGEM based detectors is not particularly reduced, and due to the enlarged geometrical parameters, they cannot offer space resolution as fine as GEM based detectors. Thanks to the reduced gaps between the multiplication stages, THGEM based detectors can be successfully used in magnetic field. These features, shortly mentioned above, match very well the requirements of specific applications in fundamental research, where the large gain, the robustness, the production technique and the mechanical characteristics are advantages, while the material budget and the space resolution aspects do not represent a limit. THGEMs are considered for the single photon detection in Cherenkov imaging applications, as active elements in hadron sampling calorimetry[15], for muon tracking[16] and for the read-out of noble liquid detectors[17].

3. The THGEM-based photocathodes of the photon detectors for the upgrade of COMPASS RICH-1

Novel MPGD-based photon counters with a hybrid architecture formed by two layer of THGEMs and a layer of MM (Fig.2) have being developed and built[18] for the upgrade of COMPASS[19] RICH-1[20], implemented in 2016. The first THGEM acts as photocathode substrate and its upper surface is coated with a thin (60 nm) CsI film. CsI has non negligible Quantum Efficiency (QE) in the far UV domain, at photon wavelength shorter than 210 nm. The effective QE in gas atmosphere has been studied by several authors[21] and proven by the RD26 development[1] and the use of MWPCs with CsI photocathodes in several experiments[22, 20]: adequate gas atmosphere is required as well as the presence at the photocathode surface of an electric field exceeding 500 V/cm. CsI is chosen because, among the typically used solid state photoconverting materials, it is definitively the most robust one, thanks to a work function higher than the other frequently used photon converters, in particular the ones with QE in the visible-light range. CsI also exhibits a relative chemical robustness against oxygen and water, as compared to other photoconverters, especially visible-sensitive ones: its QE is preserved in case of short exposure to air, namely to oxygen and water vapour, while, on a term basis of years, it can tolerate the exposure to atmospheres with oxygen and water vapour contamination at the level of a few ppm[23].

It is relevant to notice that the configuration adopted for the upgrade of COMPASS RICH-1 is the reflective photocathode one, which is preferred compare to the architectures with semitransparent photocathode, as it re-

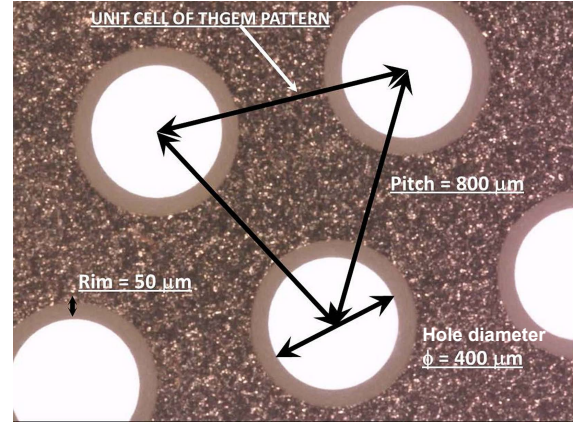


Figure 1: Detail of a THGEM PCB (picture).

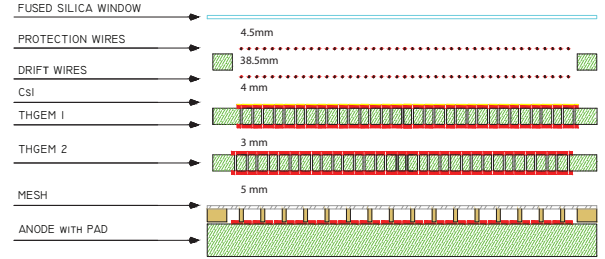


Figure 2: Scheme (not to scale) of the hybrid detector architecture for the COMPASS RICH upgrade. It includes two staggered THGEM layers (thickness: 0.4mm; hole diameter: 0.4mm; pitch: 0.8mm), and a MM (128 μ m gap, multi-pad anode).

sults in a larger photoconversion rate. In fact, a semi-transparent one requires the application of a thin metallic film, which absorbs photons, to keep the entrance window at a fix potential; also the probability of photoelectron absorption is lower in a reflective photocathode than in a semitransparent one as the conversion probability is the highest at the entrance surface of the photoconverter. Moreover, the thickness of the coating layer is largely non critical in the reflective configuration and this fact opens the way to the realization of large surface detectors.

The hybrid MPGD photon detector IBF rate is at the 3% level and it can be operated at gains higher than 10^4 [24]. The photoelectron extraction properties have been already studied by indirect measurements and are further investigated by the measurements reported in the present article.

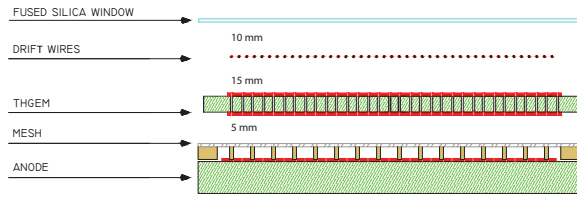


Figure 3: Scheme of the hybrid detector including a THGEM used for the measurements described in this article (not to scale).

4. Equipment and setup

4.1. The scanning system and the setup

The capability of the Leopard scanning system of performing high resolution scanning of THGEMs providing independent gain and efficiency maps by the detection of single photoelectrons has been proven[13]. The nickname "Leopard" has risen from the first images, where the photon-yield map looks like the fur marks of the wild animal. After the first principle tests, the system has been upgraded. In the following, we describe the system version used for the measurements reported in the present article.

The Leopard system consists of a pulsed UV light source with a focusing optics, mounted onto a three-dimensional moving table, and a fast data acquisition and control system reading a single channel ADC digitizing the amplified signals from the detector housing the THGEM under study. The **light source** is an LED providing 245 nm wavelength light⁴. The size of the light-spot is dictated by a dedicated pinhole. The measurements reported in the present paper have been performed with a 150 μm pinhole, resulting in a spot with a FWHM size of 7 μm . By adequate setting of the intensity of the LED light, photoelectrons can be extracted from gold- or copper-coated surfaces and the single photoelectron mode can be established: for this purpose the light intensity is tuned in order to have no more than some percent of non-empty events per pulse; for instance, the typical rate of non-empty events for the measurements reported in the present article is 5%. The stability of the intensity of the light source has been studied: the intensity is stable within the 2% level over periods of 24 h.

The light enters the detector via a fused silica window and it is focused onto the top of the **THGEM**. The extracted photoelectrons are driven by the electric dipole

field due to the THGEM voltage polarization into the nearest hole. Here they are amplified. The signal obtained by this single amplification stage is too small for effective detection and a second amplification stage is provided by a **MM**. A scheme of the hybrid MPGD used for the measurements described in this article is shown in Fig.3. The gas mixture $\text{Ar}:\text{CH}_4 = 30:70$ was used for most of the measurements (Sec. 8.1), except for the overnight ones when $\text{Ar}:\text{CO}_2 = 30:70$ was used because of safety considerations. The detector has been operated at gains in the range $1\text{--}2 \cdot 10^4$, unless explicitly mentioned. The MM anode plane is segmented in strips (400 μm pitch, 20 μm width) connected in parallel to the single read-out chain in use: the read-out area is $20 \times 60 \text{ mm}^2$. The read-out chain is formed by a preamplification stage followed by amplification.

4.2. The control and data acquisition system of the scanning system

The control system of the Leopard scanning system must ensure the adequate synchronizing among the Data Acquisition (DAQ) system, the data storage, the actuator system, with the three-dimensional movements of the light-source and the related optical setup, and additionally set detector parameters as well.

Measurement points in steps much smaller than the typical dimensions of the structure under study are required to obtain detailed images. For instance, the typical space-step, along two orthogonal axes, of the measurements reported in the present article is, for both axes, 100 μm , resulting in 10^4 measured points per cm^2 . Thousands of triggers in each measurement point are needed to get, point by point, a sample adequate for the extraction of the gain and the efficiency. Typically, we have collected point to point spectra with about 1000 entries, roughly corresponding to 20 thousand triggers per measured point. These requirements demand recording billions of events: therefore, the DAQ acquisition rate is crucial.

The control and high-rate DAQ functions are performed by a RaspberryPi⁵ microcomputer coupled via its General-Purpose Input/Output (GPIO) to a dedicated board. The board receives the asynchronous trigger whose delayed rising edge serves as selection time for a 12-bit ADC (LTC1415⁶) measuring the signal from the chamber, and the ADC is read out directly by the RaspberryPi via the GPIO. Missed triggers are counted, thus

⁴Senson Technology Inc. UVTOP-240 www.s-et.com, <http://www.s-et.com/spec-sheets/240nm-with-images.pdf>

⁵RaspberryPi, <http://www.raspberrypi.org/>

⁶Linear Technology, LTC1415, <http://cds.linear.com/docs/en/datasheet/1415fs.pdf>

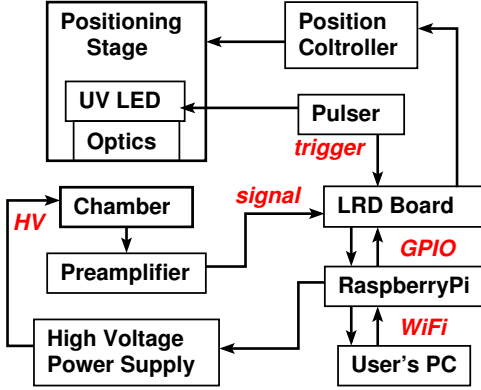


Figure 4: Block diagram of control and DAQ of the scanning system [14].

Table 1: List of the THGEMs used for the measurements reported in the present article; the geometrical parameters of the devices are provided.

THGEM	Hole	Pitch	Thickness	Rim
Name	diameter [μm]	[μm]	[μm]	[μm]
M1-III	400	800	400	0
DESTRO-I	400	800	400	5
C3HR-II	400	800	400	50
M2.4-G	400	800	600	0
M2.1-II	300	800	400	0

allowing digital signal processing at software level. An event rate of 130 kHz has been used for the measurements described in this article.

The control and DAQ software runs on the RaspberryPi under a standard Debian based Raspbian linux system. The source is written in C/C++ to make it both fast and flexible. The program accepts as inputs command lines and settings files, making convenient its remote handling. The DAQ program is also accessible by a graphical user interface, which runs on a distant machine, via intranet communication, where wireless connection is used to eliminate ground loops from Ethernet cables. A block diagram of control and DAQ system is presented in Fig. 4.

4.3. The measured thick GEMs

The measurements reported in this article refer to the THGEMs listed in Table 1, where their geometrical parameters are reported.

5. Measurement procedures

The (x,y,z) reference adopted in the following has been chosen such that the (x,y) plane is parallel to the THGEM surface, with the y-axis parallel to a row of hole centres and the z-axis orthogonal to the THGEM surface.

5.1. Algorithms for gain and yield extraction

In case of multistage detectors the distribution of the avalanche amplitude is mostly defined by the first amplification process. Operating the THGEMs at moderate gain, the expected amplitude distribution is exponential and this is the dominating distribution in our setup, as it has been crosschecked in the data.

Therefore, in the following, we assume a simple exponential distribution; in this case the most important parameters can be computed with small uncertainties even with limited statistics, as the ones we have collected in each point. We define the yield (Y) as the detected number of photoelectrons, namely the number of hits above the threshold set at a level of five standard deviation of the electronics noise distribution. The gas gain (G) can be calculated from the average or from the median of the amplitude distribution of these hits, when the threshold value is known. Knowing G , the total number of photoelectrons (Y_{extr}) can be computed by a proper extrapolation. The simple equations we use are reported in the following, where Q is the signal amplitude, Q_{cut} is the threshold value, $S(Q)$ is the amplitude distribution, N is the integral of $S(Q)$ over the whole range, Θ is the Heaviside function, and $Med[a : b]F$ refers to the median of the distribution F in the range $[a : b]$.

$$S(Q) = \frac{N}{G} \cdot e^{-Q/G} \cdot \Theta(Q) \quad (1)$$

$$Y = \int_{Q_{cut}} S(Q) dQ = N \cdot e^{-Q_{cut}/G} \quad (2)$$

$$Y_{extr} = \int_0 S(Q) dQ = N = Y \cdot e^{Q_{cut}/G} \quad (3)$$

$$Q_{med} = Med[Q_{cut} : \text{inf}](S(Q)) \quad (4)$$

$$G = \frac{1}{\ln 2} (Q_{med} - Q_{cut}) \quad (5)$$

A key ingredient to study the THGEM performance on a hole-by-hole basis is the assignment of the correlation between an illuminated point and the THGEM hole where the photoelectron drifts and initiates the avalanche process. The adopted strategy is straightforward: when a point of the THGEM surface is illuminated, the measured G is related to the nearest hole.

As a result, the area related to a hole has a hexagonal shape; this area is referred to as hole-area in the following. This choice is supported by electrostatic considerations: due to the symmetry of the THGEM geometry the field lines originated at one of the THGEM surfaces and ending at the other surface enter the nearest hole. Moreover, the two-dimensional (x, y) images obtained with poor uniformity THGEMs, as, for instance, the one shown in [13], Fig. 15, clearly indicate that the measured G-maps support our strategy.

5.2. Image focusing

In order to ensure high measurement resolution, whenever a THGEM plate is installed, the focal height of the scanning table is set. For this purpose, following the procedure already described in [13], an (y,z) scans through a line of holes is performed, where the sharpest images indicates the best focal settings. The scan outcome for one of the settings is shown in Fig. 5, where, for each (y,z) point, the yield normalized to a fix number of triggers is reported. The resolution in the focal plane determination is of the order of 1 mm. This is confirmed by the two-dimensional (x,y) images taken at z-values near the focal setting (Fig.6).

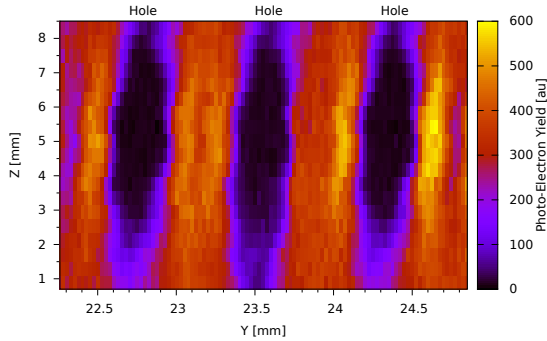


Figure 5: Image focusing by a two-dimensional scan in the (y,z) plane; for each (y,z) point, the yield normalized to a fix number of triggers is reported.

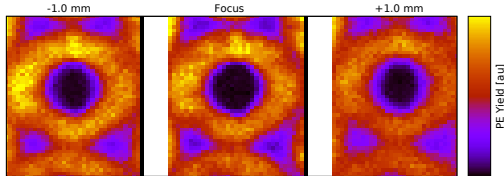


Figure 6: Yield maps at focus and slightly outside focus. It can be noticed that the change in image sharpness is limited within ± 1 mm around the best focal settings.

5.3. Estimation of the errors

The statistical errors on the measured quantities, namely G , Y and Y_{extr} , which are extracted from spectra using 20.000 events with about 400-1000 photo-electron hits, are typically at the 5%, 5% and 10% level, respectively.

Y and Y_{extr} are affected by systematic errors related to the variation of the light intensity, which is stable at the 2% level (Sec. 4).

The most relevant systematic error affecting G is due to the effects of time evolution of the gain discussed in Sec. 6 and dedicated strategies are implemented to limit the error size, when data dedicated to gain-maps are collected. The relevant systematic error for these studies is the one introducing point-to-point gain variations. By repeated measurements, we estimate that the residual relative systematic error is around the 5% level.

The correct assignment of the measurements to the corresponding hexagonal hole area (Sec. 5.1) is critical only for measurements performed at the edges of the hexagons in tiny perimetral corridors that have a width dictated by the light spot size at the THGEM surface, namely $7\mu\text{m}$ FWHM (Sec. 4). This effect is neglected in the data analysis.

6. Charging-up aspects

6.1. The time evolution of the gain in THGEM multipliers

Dedicated studies had been devoted to understand the time-evolution of the gain in THGEM multipliers [11].

The time evolution of the THGEM gain exhibits two distinct phenomena: a fast evolution, which is exhausted over time ranges between a few minutes up to about twenty minutes and a long-term time evolution, which develops over days. Both effects depend on the amount of the open dielectric surface present in the multiplier, which is related to the geometrical parameters. The former is due to the charge accumulation at the free dielectric surface present in the detector, namely the so-called charging-up: the resulting charge distribution and the time required to reach the asymptotic configuration depend on the THGEM geometry, the applied voltage and the irradiation rate; the charge accumulated at the free dielectric surface always reduces the electric field and thus the detector gain. The long-term time evolution is the more delicate aspect because of the relevance of the effect and of its time-scale: depending on the THGEM geometry, the gain decreases or increases and variations up to factors as large as 5 and even more

have been observed; stable conditions are reached after biasing the multipliers over days. This feature can be explained in terms of the charge mobility inside the dielectric, which modifies the electric field.

6.2. Gain time evolution observed with the Leopard setup

Charging up processes have been observed during the performed Leopard measurements, in particular the focus light-source allows to measure the single hole charging-up, as illustrated in Fig.7.

When a THGEM is biased for long enough time, a second phenomenon is observed: the yield increases and this effect is stronger in the large-rim THGEM C3HR-II. A tentative explanation is the stronger electric field due to the motion of charges inside the dielectric, which reinforces the electric field when a large rim is present and thus favours the photoelectron extraction. The systematic studies to explore the yield variation are not part of the present paper.

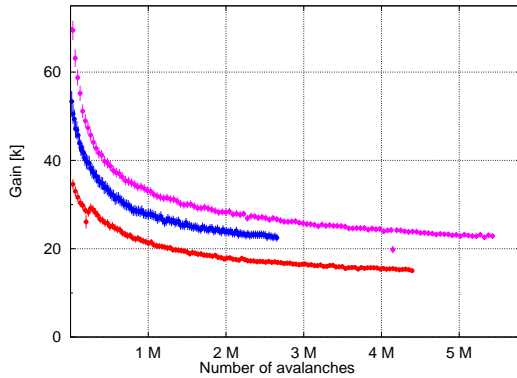


Figure 7: Charge-up curves for three different single hole in THGEM DESTRO-I; a statistic of one million events is collected in approximately 5 minutes.

The gain variation by charging-up represents a systematic effect that affect the measurements. This effect has been partially reduced by two strategies: biasing the THGEM for several hours before long-lasting measurements and illuminating the area to be measured with unfocused UV LED light before starting a measurement. The residual systematic error on G related to the charging-up effect is estimated by repeated measurements to be at the 5% level.

7. Gain studies

7.1. Gain uniformity by comparing single hole gain

Figure 8 presents the 2-D gain-map for a portion of the DESTRO-I THGEM sample. Each point at which the measurement is performed is associated to the nearest hole; in fact, in the large majority of the cases, the detected photoelectron is guided by the electric field to the nearest hole. The resulting regions associated to the holes are hexagons. The mean value of the gain measured in each hexagonal region is reported in the gain map. The gain-value is dictated by the gain in the hole and by the multiplication in the MM portion below the hole itself. A marked pattern of different gain-values is observed: in Fig. 8 the columns of hexagonal areas that are labelled with numbers "0", "3" and "6" exhibit lower gain holes, which appear with regular periodicity, while the gain is almost constant in the other columns (Fig. 9). There is full correlation between the lower gain holes and the location of the pillars supporting the micromesh in the MM, which are dead areas of the MM itself. The distribution of the hole-gain for the columns "1", "2", "4" and "5" is shown in Fig. 10; the distribution r.m.s. as provided by the gaussian fit is 6.5%, indicating an extremely good uniformity of the gain from this hole-by-hole study. A second distribution is plotted showing the gain of holes fully aligned with the pillars: the resulting gain is approximately 60% of that of holes far from the pillars.

7.2. Gain uniformity versus radial distance from the hole centre

Electric field calculation demonstrates that inside a hole of the THGEM the electric field is not constant radially. Therefore, the average gain for an avalanche produced by a single electron depends on its radial position at the hole entrance. Moreover, for the photoelectrons emitted from the converter at the THGEM surface, the same electrostatic calculations suggest that, the further the photoelectron is produced, the closer to the center of the hole it goes. The diffusion of electrons along the drift path and in the avalanche process smears the effect. A further element of complexity is the realistic calculation of the electric field in presence of charging up effects and charge displacement in the dielectric material. An experimental investigation of the gain variation versus the radial distance from the hole centre of the point where the photoelectron has been generated can be addressed with the Leopard setup within the space resolution provided by the size of the focus light-spot.

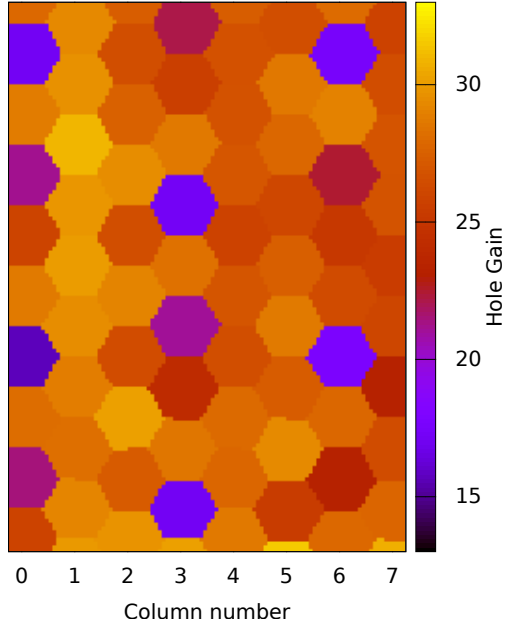


Figure 8: Map of hole-gain for a portion of the DESTRO-I THGEM sample. The hexagonal regions correspond to the hole-areas. The columns of hexagonal areas are labelled with numbers.

Dedicated fast scans have been performed on previously illuminated small areas, thus avoiding the systematic effect due to charging-up and -down of the studied surface. For each of the holes, the gain of all hole-area points, normalized to the hole-gain defined as the average gain of all the point of the hole-area, have been combined together: the result is shown in Fig.11. The measured distribution is flat within uncertainties, however does not exclude a moderate increase of the gain for the photoelectrons generated far from the hole, which drift towards the center of the hole itself.

8. Photoelectron extraction studies

8.1. The effective quantum efficiency in gaseous detectors

The effective QE obtained in a gaseous detector depends on the gas used and the electric field at the photocathode surface. When the photoelectron elastically scatters off a gas molecule, the back-scattering probability is high and part of the photoelectrons impinge back on the photocathode where they are absorbed. Therefore, the effective QE is reduced. The characteristics of the gas molecules and the value of the electric field accelerating the photoelectrons determine the elastic scattering rate and thus the effective QE. Both parameters

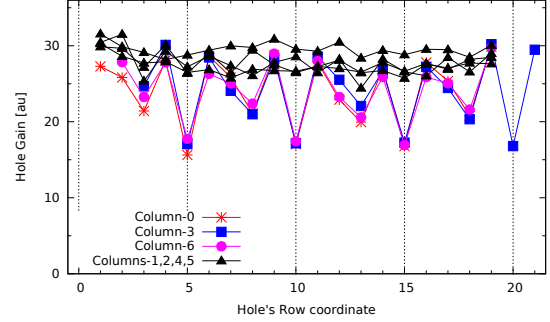


Figure 9: Hole-gain for the different hole-areas of the seven columns indicated in Fig. 8.

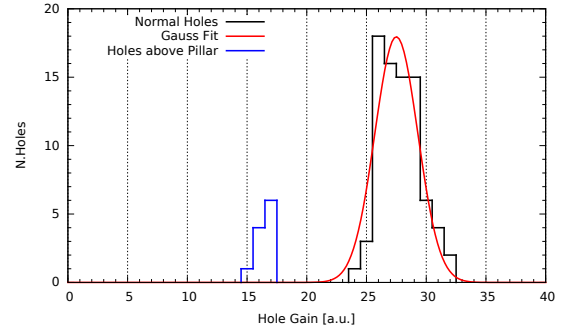


Figure 10: Hole-gain distribution for the DESTRO-I THGEM sample; black line: holes in the columns "1", "2", "4" and "5"; red line: gaussian fit of the distribution; blue line: holes fully aligned with MM pillars.

have been studied in the context of RD26[25, 26] and newly explored recently[12, 27]. The response in different gas atmospheres has also been reproduced by simulations[26, 28]. An example of the measurements performed is shown in Fig. 12. At atmospheric pressure, the effective quantum efficiency increases very steeply up to electric field values of about 1000 V/cm. At higher field values, the increase rate versus field is reduced, even if it remains non-negligible. The highest quantum efficiency is obtained in pure methane or in methane-argon mixtures, provided that the methane fraction is high (> 40%).

A major question is the possibility to have good effective quantum efficiency on the whole reflective photocathode surface of a THGEM device. The field at the photocathode surface is the combination of the dipole field due to the voltage applied between the two THGEM faces and the external additional field, applied between the CsI coated THGEM face and an electrode placed above this surface, usually referred to as drift field in the literature. The contribution of the dipole

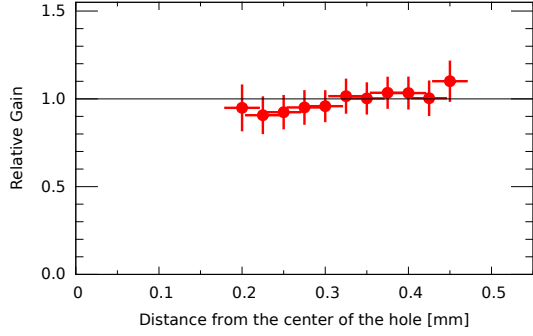


Figure 11: Relative gain versus the radial distance of the photoelectron emission point from the hole centre for THGEM DESTRO-I.

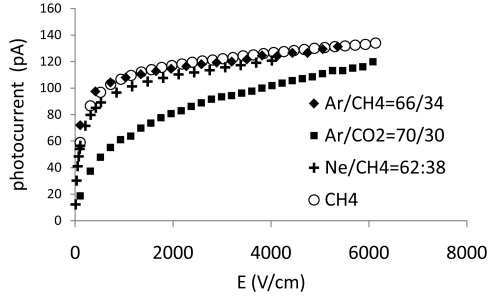


Figure 12: CsI photocurrent versus applied electric field in various gases and gas mixtures at atmospheric pressure; systematic uncertainty at the 1% level[12].

field results in a field pointing towards the photocathode surface, with variable intensity and orientation at different surface points.

The drift field is called direct when pointing outward from the THGEM surface, this being the direction used in tracking applications, and reversed when pointing toward the THGEM top surface. In this article positive values are assigned to the direct field and negative values to the reversed field. When a reverse drift field is applied, part of the photoelectrons are collected at the electrode above the photocathode and they do not enter the multiplication chain: they are lost. The direct drift field contributes in guiding the electrons towards the amplification holes. In this configuration the electric field accelerating the extracted photoelectrons is the combination of the dipole field and the drift field. Therefore, the optimal drift field value is the one providing at the same time, the effective guidance to the electrons toward the holes and sufficient photoelectron acceleration.

A first optimization study has been performed measuring photocurrents[12]. A single THGEM layer with CsI coating illuminated with a UV lamp has been used

and the current at the detector anode has been measured. The plots in Fig. 13 clearly indicate a sharp current decrease for reversed drift field, as expected, and a rough plateau for moderate values of the direct drift field, followed by a drop when the total field pushes the photoelectrons back to the photocathode. Moreover, the current drops at lower values of the direct drift field when the dipole field is lower, as intuitively expected. This observation confirms the relevance of a high dipole field. These first measurements, even if confirming the global picture, suffer of a systematic limitation: the measured currents depends both on the the number of extracted photoelectrons and the gain, which is not constant varying the drift field.

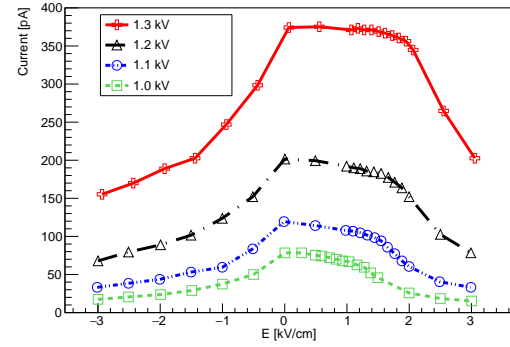


Figure 13: Anode current measured in a single THGEM detector with CsI reflective photocathode versus the additional electric field applied; the different point sets have been obtained for different values of the potential ΔV applied between the THGEM faces[12].

Electrostatic calculations also indicate that higher dipole field at the THGEM surface can be obtained increasing the ratio R of the hole diameter to the hole pitch. At the same time, when R is large, the fraction of the THGEM surface that can be coated is reduced; for $R = 0.5$, this fraction is 77%. The two competing requests dictate a strong constrain on the ratio value and suggest to adopt geometries with $R=0.5$.

8.2. Direct observation of the effective quantum efficiency using THGEM as photocathode substrate

Images obtained with the Leopard setup provide a deeper understanding of the role of the drift field. When the drift field is optimized, photoelectrons from the whole THGEM surface are effectively extracted and multiplied. The relevant plots are 2-D Y_{extr} -maps. The studies illustrated in this subsection have been performed using the THGEM M1-III. The same number of events has been collected at each point, thus making the

results within a map and those related to maps obtained in different conditions directly comparable.

Figure 14 presents a the Y_{extr} -maps obtained for fixed THGEM bias voltage varying the drift field. The maps indicate as optimal range for the drift field the range 200-500 V/cm of the direct field.

The Y-maps and Y_{extr} -maps obtained for two fixed value of the drift field varying the THGEM bias voltage are shown in Fig. 15. The typical noise value during these measurements is around 2300 electrons equivalent. The corresponding 5- σ threshold value is 11500 electrons equivalent. The resulting detection efficiency is about 30% at a gain of 10k gain obtained at 1660 V and larger than 72% at a gain of 36k obtained at 1850 V. The Y_{extr} -maps show that, in spite of the relevant variation of the detector total gain, no relevant variation of the effective quantum efficiency is observed when the optimized drift field is applied. At the same time, the Y-maps underlay the relevance of operating at high detector gain when the noise level imposes high threshold values of the read-out front-end electronics.

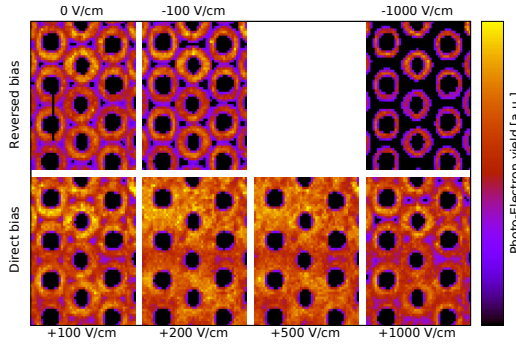


Figure 14: Y_{extr} -maps for fixed THGEM bias voltage varying the external drift field applied in front of the photocathode.

The electric field configuration at the THGEM surface is particularly low at the points which are at equal distance from the three nearest holes resulted from simple symmetry considerations. Correspondingly, it is expected that the photoelectron extraction is more problematic at this Critical Points (CP). The expectation is confirmed by the images in Fig. 15, where it can also be observed that, for optimized values of the drift field, the inefficiency at the CPs is overcome. The rapid evolution of the photoelectron extraction efficiency at the CP is illustrated in Fig. 16.

The photoelectron extraction efficiency can also be studied with a quicker approach which does not require two-dimensional scans: one-dimensional scans along lines connecting a row of CPs, critical line, are performed. Figure 17 presents a set of seven one-

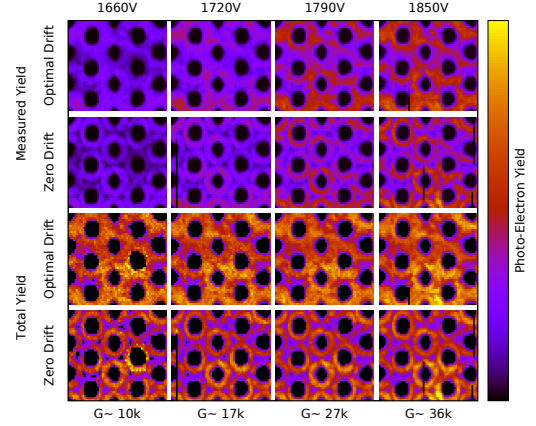


Figure 15: The Y-maps and the Y_{extr} -maps obtained applying two fixed value of the drift field (0, optimal drift field: 200 V/cm) and varying the THGEM bias voltage, which results in an important variation of the detector gain, as indicated.

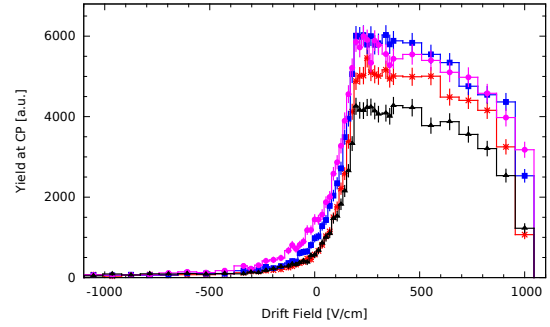


Figure 16: The photoelectron yield at four different CPs versus the applied drift field.

dimensional scans obtained by varying the drift field; where the the critical line crosses three holes and four CPs. The results of scans along the same critical line varying the drift field are summarized in Fig. 18, B: the region of optimal drift field and the photoelectron yield evolution along the critical line are clearly visible.

8.3. Comparison of the photoelectron extraction in THGEMs with different geometry.

One-dimensional scans along a critical line varying the applied drift field have been performed for THGEMs with different geometrical parameters. The results are presented in Figs 18, A for THGEMs M2.4-G and C for THGEM M2.1-II. These plots have to be compared with the one presented in Fig. 18, B obtained using THGEM M1-III.

THGEM M2.4-G is thicker than THGEM M1-III; in a thicker THGEM, a larger fraction of the dipole electric

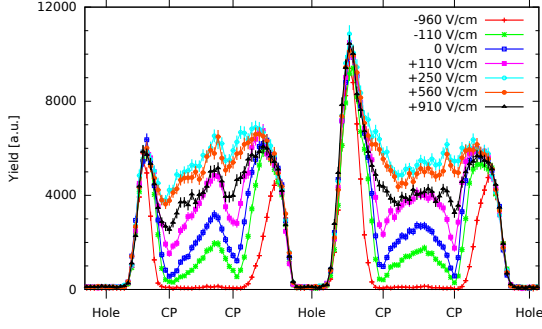


Figure 17: Y_{extr} from the one-dimensional scan along a critical line portion, including three holes and four CPs, for seven different values of the drift fields.

field is confined in the holes and the high field region, where the multiplication takes place, is longer. Therefore, larger gain can be obtained. At the same time, it can be expected that the photoelectron extraction at the CPs is more marginal because the dipole electric field is more feeble there. This aspect is not confirmed by our measurement: THGEM M2.4-G geometrical parameters are as valid as the ones of THGEM M1-III.

In THGEM M2.1-II, the hole diameter is smaller than in THGEM 1-III; also in this case, a larger fraction of the dipole electric field is confined in the holes and expectations are similar to those of the previous case: higher gain and more difficult photoelectron extraction at the CPs. The plots indicate that complete photoelectron extraction is possible also for this geometry, even if the range of optimal drift field values is more limited. This indication is of particular interest because, thanks to the reduced R value of THGEM M2.1-II ($R = 0.375$) the surface available for CsI coating is larger: 87% to be compared with the value of 77% for THGEM M2.1-III. Therefore, THGEMs with M2.1-II geometrical parameters can be considered as photocathode substrates in MPGD-based photon detectors.

9. Photoelectron extraction from CsI and from gold in gaseous atmosphere

The measurements described in Sec. 8 have been performed extracting photoelectrons from gold-coated surfaces. The gaseous photon detectors are operated with CsI photoconverters. Therefore, we have performed a set of measurements to establish the portability of the results described in the previous sections to the gaseous photon detectors as operated in experiments. For these purposes we have compared measurements performed

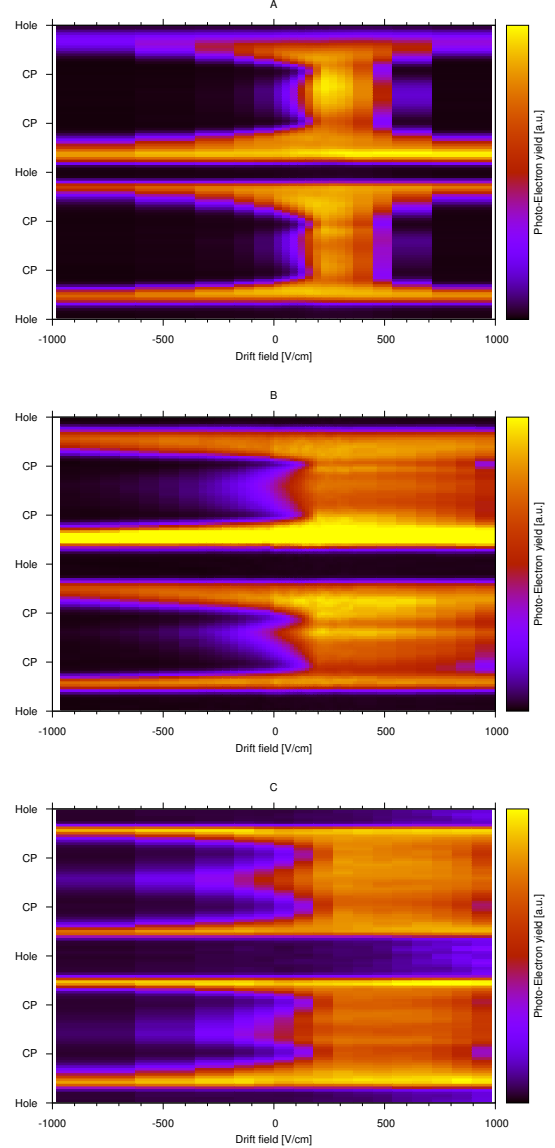


Figure 18: Y_{extr} from the one-dimensional scans along a critical line (y-axis) varying the drift field (x-axis). Three different THGEMs have been used: M2.1-II (A), M1-III (B), M2.4-G (C).

extracting photons from gold and from CsI using argon-methane gas mixtures.

Two parallel plates are housed in a chamber filled with the appropriate gas mixture and a voltage bias between them is applied. The plate acting as photocathode is by fiberglass and it is coated with a layer of 35 μm of copper and superimposed layers of nickel (5 μm) and gold (0.5 μm); one more layer of CsI, 300 nm thick, has been added to the CsI-photocathode. The light from a

deuterium lamp⁷ is guided via a quartz fibre to the photocathode and the light impinges on it at 45°. The current generated by the extracted photoelectrons is measured with a picoammeter⁸. Results are presented in Fig. 19 for Ar:CH₄=60:40. The ratio of the anode current versus the electric field measured using the CsI coated cathode and the gold coated one exhibits a very modest increase for increasing values of the electric field. This behavior indicates that the results concerning the photoelectron extraction from THGEM photocathodes obtained with the gold coated THGEMs can be extended to the THGEMs with CsI coating, even if the dependence of the photoelectron extraction on the electric field is slightly more marked when CsI is present.

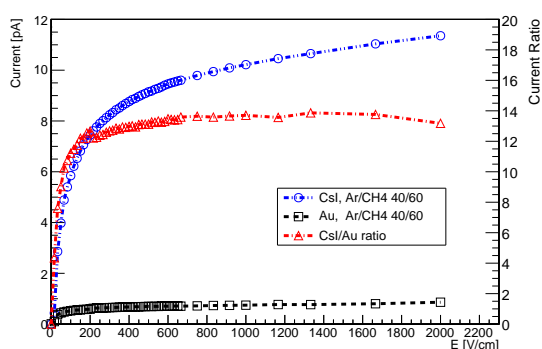


Figure 19: Current measured at the anode while illuminating the CsI coated cathode (circles) and the gold coated cathode (squares) versus the electric field in Ar:CH₄ = 60:40 atmosphere; the ratio of the two currents is also shown (triangles).

10. Conclusions

Direct measurements of the properties of THGEM reflective photocathodes have been performed scanning THGEM surfaces by a high resolution optical system and detecting photoelectrons.

The results of this laboratory investigation concern the THGEM gain uniformity in hole-by-hole measurements and versus the distance from the nearest hole, photoelectron extraction with particular care dedicated to the extraction location, the biasing voltage applied to the THGEM, the electric field above the photocathode surface and the extraction properties of THGEMs with different geometry. The direct measurement confirm the indication provided by precedent indirect measurements.

⁷Oriel type 63162

⁸Keithley type 6485

Photoelectron extraction from CsI-coated and from gold-coated photocathodes in gaseous atmosphere have been compared. It is so possible to extend the results obtained for gold-coated THGEMs to CsI coated devices.

The results have provided precious information to guide the design, construction and operation of gaseous photon detectors where THGEMs are used as photocathode substrates.

Acknowledgments

This work has been performed in the framework of the RD51 collaboration and the COMPASS RICH-1 upgrade; the authors are grateful to the Colleagues of both collaborations for constant support and encouragement.

The activity is supported in part by the European Community, within the H2020 project AIDA-2020, GA no. 654168.

References

- [1] RD26 Collaboration, status reports: CERN/-DRDC 93-36, 94-49, 96-20; The ALICE collaboration, Technical Design Report of the High Momentum Particle Identification Detector, CERN/LHCC 98-19, ALICE TDR 1, 14 August 1998; F. Piuze, Ring Imaging Cherenkov systems based on gaseous photo-detectors: Trends and limits around particle accelerators, Nucl. Instr. and Meth. A 502 (2003) 76.
- [2] F. Sauli, GEM: A new concept for electron amplification in gas detectors Nucl. Instr. and Meth. A 386 (1997) 531.
- [3] L. Periale et al., Nucl. Instr. and Meth. A 478 (2002) 377; P. Jeanneret, PhD thesis, Neuchatel University, 2001; P.S. Barbeau et al, IEEE NS-50 (2003) 1285; R. Chechik et al, Nucl. Instr. and Meth. A 535 (2004) 303.
- [4] Y. Giomataris et al., Nucl. Instr. and Meth. A 376 (1996) 29.
- [5] M. Alexeev et al., JINST 8 (2013) P01021.
- [6] Upgrade of the ALICE Time Projection Chamber. Technical Report CERN-LHCC-2013-020. ALICE-TDR-016, CERN, Geneva, October 2013
- [7] W. Anderson et al., Nucl. Instr. and Meth. A 646 (2011) 35.
- [8] A. Breskin et al., Nucl. Instrum. Meth. A 598 (2009) 107 and references therein.
- [9] A. Di Mauro et al., Nucl. Instrum. Meth. A 639 (2011) 274.
- [10] M. Alexeev et al., Nucl. Instr. and Meth. A 610 (2009) 174; M. Alexeev et al., Nucl. Instr. and Meth. A 617 (2010) 396; M. Alexeev et al., 2010 JINST 5 P03009; M. Alexeev et al., Nucl. Instr. and Meth. A 639 (2011) 130; M. Alexeev et al., 2012 JINST 7 C02014; M. Alexeev et al., Nucl. Instr. and Meth. A 695 (2012) 159; M. Alexeev et al., Physics Procedia, 37 (2012) 781; M. Alexeev et al., Nucl. Instr. and Meth. A 732 (2013) 264; M. Alexeev et al., 2013 JINST 8 C12005; M. Alexeev et al., 2014 JINST 9 C03046; M. Alexeev et al., 2014 JINST 9 C09017; M. Alexeev et al., Nucl. Instr. Meth. A 766 (2014) 133; M. Alexeev et al., PoS (TIPP2014) 075.
- [11] M. Alexeev et al., 2015 JINST 10 P03026.
- [12] M. Alexeev et al., Nucl. Instr. and Meth. A 623 (2010) 129.
- [13] G. Hamar and D. Varga, Nucl. Instr. and Meth. A 694 (2012) 16.
- [14] G. Hamar and D. Varga, Proc. of Science TIPP2014 (2015) , 056
- [15] S. Bressler et al., JINST 8 (2013) P07017.

- [16] K. Gnanvo et al., Nucl. Instr. and Meth. A 652 (2011) 16.
- [17] C. Cantini et al., JINST 10 (2015) P03017.
- [18] M. Alexeev et al., Status of the Development of Large Area Photon Detectors based on THGEMs and Hybrid MPGD architectures for Cherenkov Imaging Applications, Nucl. Instr. and Meth. A 824 (2016) 139; M. Alexeev et al., The MPGD-based photon detectors for the upgrade of COMPASS RICH-1, Nucl. Instr. and Meth. A 876 (2017) 96; M. Alexeev et al., Status of COMPASS RICH-1 Upgrade with MPGD-based Photon Detectors, EPJ Web of Conferences 174 (2018) 01004; M. Alexeev et al., Status of COMPASS RICH-1 Upgrade with MPGD-based Photon Detectors, EPJ Web of Conferences 174, (2018) 01004; J. Agarwala et al., The MPGD-based photon detectors for the upgrade of COMPASS RICH-1 and beyond, Nucl. Instr. and Meth. A 936 (2019) 416; J. Agarwala et al., The hybrid MPGD-based photon detectors of COMPASS RICH-1, Nucl. Instr. and Meth. A (2019), <https://doi.org/10.1016/j.nima.2019.01.0>.
- [19] The COMPASS Collaboration, P. Abbon et al., Nucl. Instr. and Meth. A 577 (2007) 455; The COMPASS Collaboration, P. Abbon et al., Nucl. Instr. and Meth. A 779 (2015) 69.
- [20] E. Albrecht, et al., Nucl. Instr. and Meth. A 553 (2005) 215; P. Abbon et al., Nucl. Instr. and Meth. A 587 (2008) 371; P. Abbon et al., Nucl. Instr. and Meth. A 616 (2010) 21; P. Abbon et al., Nucl. Instr. and Meth. A 631 (2011) 26.
- [21] A. Breskin et al., Nucl. Instr. and Meth. A 367 (1995) 342; M. Alexeev et al., Nucl. Instr. and Meth. A 623(2010) 129; C. D. R. Azevedo et al., 2010 JINST 5 P01002.
- [22] C.W. Fabjan et al., Nucl. Instr. and Meth. 367 (1995) 240; M. Spegel, Nucl. Instr. and Meth. A 433 (1999) 366; J. Friesen et al., Nucl. Instr. and Meth. A 438 (1999) 86; H. Rabus et al., Nucl. Instr. and Meth. A 438 (1999) 94; R. Gernhauser et al., Nucl. Instr. and Meth. A 438 (1999) 104; A. Braem et al., Nucl. Instr. and Meth. A 499 (2003) 720; F. Garibaldi et al., Nucl. Instr. and Meth. A 502 (2003) 117; M. Iodice et al., Nucl. Instr. and Meth. A 553 (2005) 231; The ALICE Collaboration, Technical Design Report of the High Momentum Particle Identification Detector, CERN/LHCC 98-19, ALICE TDR 1, 14 August 696 1998; P. Martinengo et al., Nucl. Instr. and Meth. A 639 (2011) 7.
- [23] M. Alexeev et al., JINST 9 (2014) P01006.
- [24] J. Agarwala et al., Nucl. Instr. and Meth. A 936 (2019) 416.
- [25] A. Breskin et al., Nucl. Instr. and Meth. A 367 (1995) 342.
- [26] A. Di Mauro et al., Nucl. Instrum. Meth. A 371 (1996) 137.
- [27] C. D. R. Azevedo et al., JINST 5 (2010) P01002.
- [28] J. Escada et al., J. Phys. D: Appl. Phys. 43 (2010) 065502.